ADVANCED ENGINEERING MATERIALS
www.aem-journal.com

Effects of Processing Conditions of a Ball-Milled $Fe_{65}Co_{35}$ Soft Ferromagnetic Alloy on the Structural, Thermal, and Magnetic Properties

*Jason Daza, Zaida Curbelo-Cano, Cristina M. Montero, Wael Ben Mbarek, Lluïsa Escoda, Joan Saurina, Ester M. Palmero, Alberto Bollero, Pere Bruna, and Joan-Josep Suñol**

The $Fe_{65}Co_{35}$ alloy is a well-known Fe-based soft ferromagnetic alloy with excellent soft magnetic properties, which make it a strong candidate to be used in technological applications. In the present work, synthesizing nanoscrystalline $Fe_{65}Co_{35}$ alloy by mechanical alloying is focused on, adding cyclohexane (C_6H_{12}) acting as a process control agent (PCA). PCAs are effective in favoring nanostructured alloys with uniform grain size. The production of this type of alloy is a promising approach to tune the magnetic hardness in $Fe_{65}Co_{35}$. Structural, thermal, morphological, and magnetic properties have been studied after milling for 10, 25, and 50 h with and without the PCA. In the structural analysis, it is shown that the cubic α-Fe(Co) phase is the predominant phase in all samples. The use of the PCA favors its nanocrystallinity; however, it slows Co diffusion into the Fe matrix. Thermal analysis detects an endothermic process between 525 and 575 °C in the samples milled with C_6H_{12} only. This is associated with the transition of the residual Fe_3Co superlattice, to the stable α-Fe(Co). The effect of the residual Fe_3Co at room temperature on the magnetic properties is twofold, by decreasing the saturation magnetization of $Fe_{65}Co_{35}$ but increasing both remanent magnetization and coercivity.

1. Introduction

In the everlasting quest of human evolution, new advanced materials are of paramount importance. As our technological world continues to expand, the urge to develop suitable materials is present. Among these new and necessary materials are the soft ferromagnetic alloys. Soft ferromagnetic alloys are characterized by their high saturation magnetization and low coercivity.[1] Understanding their structural and thermal behavior is crucial to fully comprehend the magnetic behavior of said alloys. Therefore, a structural and thermal analysis of soft ferromagnetic alloys can help to optimize their manufacturing to obtain the desired magnetic properties.

The applicability of soft ferromagnetic alloys is very wide. They have been implemented in sensors, transformer cores, and magnetic actuators.[2–5] These applications mainly use the properties of low coercivity, high saturation magnetization, and high magnetoresistance presented by these alloys.[2,6–8] However, soft ferromagnetic alloys can also be used in combination with hard magnetic materials (spring magnets) to match the complementary magnetic properties of both material types and reduce the use of critical raw materials (rare-earth elements) in the production of high-energy density magnets.[9–11] Spring magnets are composite materials that combine a soft ferromagnetic alloy (typically with about 5 wt% content) acting as the reinforcement of a hard magnetic alloy matrix. The coupling between a soft magnetic alloy with a hard magnetic alloy to produce a spring magnet enhances the wide range of applicability.

J. Daza, W. Ben Mbarek, L. Escoda, J. Saurina, J.-J. Suñol
Department of Physics, Campus Montilivi s/n
University of Girona
17003 Girona, Spain
E-mail: joanjosep.sunyol@udg.edu

The ORCID identification number(s) for the author(s) of this article can be found under https://doi.org/10.1002/adem.202402317.

[+]Present address: Advanced Technologies and Micro Systems, Robert Bosch GmbH, Corporate Sector Research, Renningen, 70465 Stuttgart, Germany

DOI: 10.1002/adem.202402317

Z. Curbelo-Cano, C. M. Montero, E. M. Palmero, A. Bollero[+]
Group of Permanent Magnets and Applications
IMDEA Nanoscience
28049 Madrid, Spain

P. Bruna
Department of Physics, Av. Eduard Maristany 16
Universitat Politècnica de Catalunya
08019 Barcelona, Spain

The range includes applications from information storage technology (magnetic recording media) to biomedical applications (magnetic resonance imaging and drug delivery).[12–14]

Fe–Co alloys are well-known soft magnetic materials with high magnetic saturations of up to 240 emu g^{-1} in bulk form,[15] a low coercivity between 10 and 65 Oe,[16] and high Curie temperatures above 1500 K,[17] depending on the atomic percentage (at%) of Co. The manufacturing of these alloys is achievable chemically or physically.[18,19] Within all the techniques, mechanical alloying (MA) can induce the formation of metastable phases and allotropic transformations[18,20] that usually occur at high temperatures.[21] In addition, MA favors the formation of nanocrystalline structures, which enhances the overall magnetic behavior of the final alloys.[22–24] Obtaining nanocrystalline alloys by mechanical alloying has been proved by other authors. The study by Berghuel et al. focused on analyzing the microwave absorption properties of a mechanically alloyed $Fe_{60}Co_{40}$ alloy. The study concluded that an average crystal size of 13 nm was obtained after 36 h of milling.[25] A similar study by Laala-Bouali et al. obtained an average crystal size of 18 nm after milling a $Fe_{70}Co_{30}$ alloy for 24 h.[26] The magnetic behavior can be reduced if a minor oxide is formed, as Fe_3O_4.[27] Regarding the exchange coupling in magnetic composites, this effect has been detected in soft magnetic Fe–Co particles mixed with hard magnetic Mn–Al.[28] The same effect has been found in $Sm(Co,Zr)_7$/FeCo magnetic composites.[29]

The present study focuses on analyzing one particular Fe–Co alloy, known for its soft ferromagnetic behavior, produced by mechanical alloying (MA). The effects of milling time and the addition of cyclohexane (C_6H_{12}) acting as a process control agent (PCA) are analyzed. The Fe–Co system is one that has been studied previously.[2,30–33] However, the effect a PCA has on the structural, thermal, morphological, and magnetic properties of the alloys of this system has not been analyzed. As proved by other studies, the main purpose of adding a PCA during milling is to favor obtaining smaller particle sizes.[34–38] Particle size has a clear effect on the soft magnetic behavior of the alloys.[22] Yazdani et al. determined that the addition of a PCA during milling prevented the solid solution formation.[34] The study by Cotai et al. found a relationship between the addition of a PCA and the saturation magnetization of the final sample.[37] However, Nouri et al. found that samples were contaminated due to the addition of a PCA.[38] In this study, the structural, thermal, morphological, and magnetic properties of a $Fe_{65}Co_{35}$ alloy manufactured with and without a PCA for different milling times have been analyzed.

2. Results and Discussion

2.1. Structural Analysis

As mentioned above, the structural analysis was performed by XRD. All of the XRD patterns are presented in **Figure 1** and the corresponding results of the analysis in **Table 1**. The Miller Indices for all the identified peaks are also presented in Figure 1. To obtain the parameters in Table 1, the lattice parameter was the first parameter to be refined. Once the lattice parameter was refined, the crystal size and the microstrain were the next parameters to be obtained. Finally, the weight percentage of each of the phases was determined.

All samples have a body-centered cubic (BCC) structure as the predominant phase. The $Fe_{65}Co_{35}$ samples milled for 10 and 25 h with PCA also present the Co hexagonal close-packed (HCP) phase. When analyzing in detail each of the characteristic peaks of the BCC structure (**Figure 2**), each presents a superposition of two peaks very close together. This superposition indicates the coexistence of two different Fe crystallographic domains with very similar lattice parameters.[39,40] Other authors define these two domains as two distinctive phases.[30,31,41] These two phases are the α-Fe(Co) phase ($Im\bar{3}m$ space group) and the B2 phase

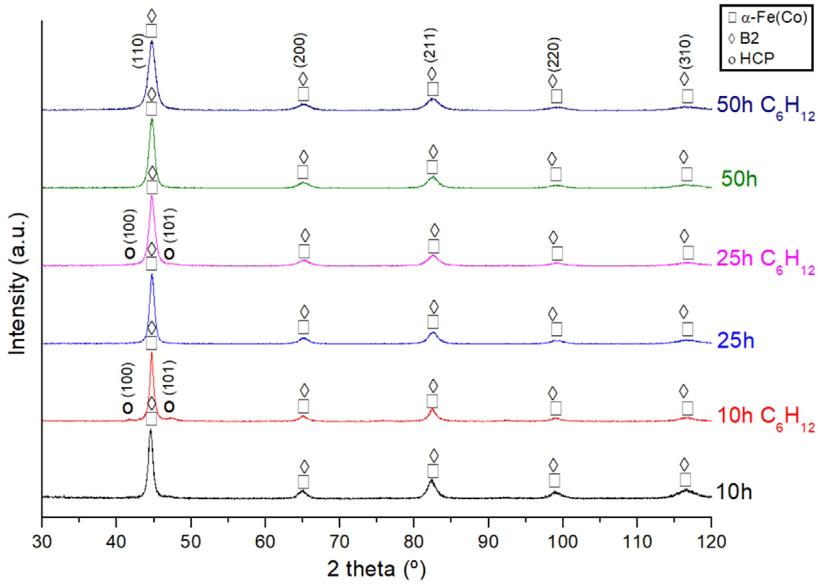

Figure 1. XRD patterns for all six samples with Miller Indices indicated and peaks identified using the corresponding CIF file for the α–Fe(Co),[39] the B2,[40] and the Co HCP[41] structures.

Table 1. XRD analysis results obtained in MAUD using the Rietveld refinement method. It includes the detected phases and their percentage, the lattice parameter (a), the crystal size (L), the microstrain (ε), the dislocation density (ρ_d), and the goodness of fit (GoF).

Sample	Phases	%Phases	a [nm]	L [nm]	ε [−]	ρ_d [nm^{-2}]	GoF
$Fe_{65}Co_{35}$ 10 h	α-Fe(Co) B2	81.42(0) 19.58(0)	0.2862(0) 0.2863(0)	23.37(37) 27.02(18)	0.00571(8) 0.00449(2)	3.41×10^{-3}(10) 2.32×10^{-3}(3)	1.013
$Fe_{65}Co_{35}$ 25 h	α-Fe(Co) B2	68.13(0) 32.87(0)	0.2863(0) 0.2865(0)	22.10(15) 25.17(36)	0.00585(2) 0.00525(3)	3.70×10^{-3}(4) 2.91×10^{-3}(6)	1.023
$Fe_{65}Co_{35}$ 50 h	α-Fe(Co) B2	59.37(0) 40.63(0)	0.2865(0) 0.2866(0)	21.94(29) 24.97(32)	0.00598(6) 0.00532(4)	3.81×10^{-3}(9) 2.97×10^{-3}(6)	1.058
$Fe_{65}Co_{35} + C_6H_{12}$ 10 h	α-Fe(Co) B2 Co-HCP	85.01(0) 1.37(0) 13.62(0)	0.2865(0) 0.2868(0) 0.2507(0) 0.4070(0)	19.63(15) 22.71(19) 10.62(17)	0.00186(9) 0.00125(3) $6 \cdot 10^{-4}$(0)	1.32×10^{-3}(7) 7.68×10^{-4}(2) –	1.072
$Fe_{65}Co_{35} + C_6H_{12}$ 25 h	α-Fe(Co) B2 Co-HCP	79.63(0) 12.68(0) 7.69(0)	0.2865(0) 0.2865(0) 0.2507(0) 0.4070(0)	16.23(11) 20.33(23) 10.26(12)	0.00427(7) 0.00377(5) $6 \cdot 10^{-4}$(0)	3.67×10^{-3}(9) 2.59×10^{-4}(6) –	1.109
$Fe_{65}Co_{35} + C_6H_{12}$ 50 h	α-Fe(Co) B2	71.29(0) 28.71(0)	0.2865(0) 0.2866(0)	13.09(10) 18.89(14)	0.00502(8) 0.00495(3)	5.35×10^{-3}(13) 2.89×10^{-4}(5)	1.096

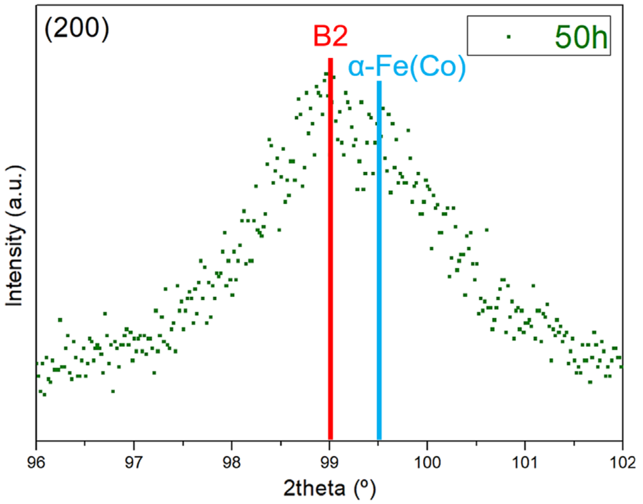

Figure 2. Enlargement of the diffractogram of the sample milled for 50 h without PCA between 96° and 102° corresponding to the (200) Miller Index. The red line corresponds to the identified peaks for the B2 phase and the blue line to the α-Fe(Co) phase.

($Pm\overline{3}m$ space group). The α-Fe(Co) phase is an α-Fe solid solution with Co atoms substituting Fe atoms in the structure. The B2 phase is a central Fe atom surrounded mainly by Co atoms. According to the phase diagram that these authors use,[41] both the α-Fe(Co) and B2 phases are stable at room temperature.

The other two peaks identified with the[42,43] Miller Indices correspond to two of the principal HCP crystallographic structure peaks. Other peaks associated with this crystallographic structure are not visible in the diffractograms of Figure 1 due to their low intensity. This hexagonal structure is associated with the Co precursor used. The elemental Co powder used in the synthesis process presents a stable HCP structure at room temperature.

The samples milled without PCA show complete diffusion of Co into the Fe matrix for all of the milling times. In these samples, XRD does not detect the HCP peaks associated with the Co precursor. However, for the samples milled with PCA, complete diffusion of Co into the Fe matrix is only achievable after 50 h of milling. For the samples milled for 10 and 25 h with PCA, XRD detects HCP peaks associated with the Co precursor.

During milling, the PCA acts as a lubricant.[34,35] Therefore, the union and diffusion of the elements in the alloy slowdown.[36–38] For this reason, only the samples milled with PCA show peaks associated with the HCP structure of the Co precursor. To obtain complete diffusion when using a PCA, milling time has to be increased. Moreover, as milling time increases, the α-Fe(Co) solid solution forms similarly to the samples produced without the PCA. Also, as milling time increases, the amount of B2 phase increases as longer milling times favor Co diffusion.

As the milling time increases, the lattice parameter (α) tends to stabilize at specific values for each of the phases (Table 1). This is true for both the samples produced with and without PCA. The main difference between the samples occurs for low milling times.

For those produced without PCA, the lattice parameter increases with longer milling times. This increase in lattice parameter is associated with the diffusion of Co into the Fe matrix. As the atomic radius of Co (0.126 nm) is larger than that of Fe (0.125 nm), a larger diffusion of Co into the Fe matrix would justify the increase of the lattice parameter. Therefore, as longer milling times favor a greater diffusion of Co into an Fe matrix, the lattice parameter increases.

The effect of the PCA on the alloy slows down the diffusion of Co into the Fe matrix. When using the PCA during the synthesis process, it would seem that the lattice parameter stabilizes around the value of 0.2865 nm. This is believed to be caused by the carbon from the PCA. During the first stages of milling (short milling times), carbon is positioned interstitially within the alloy's Fe matrix. Then, the interstitial carbon causes a distortion within the alloy by increasing the corresponding lattice parameter. As milling time increases, the interstitial carbon becomes diffused carbon. Therefore, the increase in lattice parameter due to the diffusion of Co identified for the samples manufactured without PCA is shadowed by the distortion caused by the carbon. In other words, two simultaneous processes occur. At shorter milling times, the value of the lattice parameter is determined by the interstitial carbon, while at longer milling times, it is determined by the diffusion of Co into the Fe matrix.

Elemental analysis confirms the presence of carbon in the samples processed with PCA. For the samples milled without PCA and the Fe precursor, elemental analysis detects no carbon. Therefore, it can be concluded that the carbon present in the samples milled with PCA comes from the fractioning of the C_6H_{12} during milling. The analysis was achieved by combusting the samples and checking the combustion gases. The results of the weight percentage of carbon in the samples were 0.35% for 10 h, 0.55% for 25 h, and 0.83% for 50 h, demonstrating that longer milling times favor a higher carbon content in the alloy. Longer milling times favor the diffusion of carbon into the iron matrix of the alloy, as previously discussed based on results obtained from the XRD analysis. It must be noted that the content of carbon is very low when compared to the initial amount from the C_6H_{12}. For the amount of C present in the samples, Fe_3C could be formed and detectable by XRD as a precipitate. XRD analysis does not detect Fe_3C in the samples of this study. However, in the literature, studies have been found in which cementite is not detectable by XRD when the C content is around 4 at%.[44] In the case of this study, 0.83 w% of C corresponds to ≈4 at%.

For the samples produced without PCA, the evolution of the crystal size is in accordance with the results presented by other authors (Table 1).[45,46] As the milling time increases, the average crystal size decreases. This decrease in crystal size can be explained by the hardening of the FeCo alloy as the solid solution evolves with increasing milling time. As a consequence, the reduction in crystal size is obtained by the favored grain fragmentation process induced by MA.[45,47] This effect is observed for all samples regardless of if the PCA is used or not. Moreover, the use of C_6H_{12} as a PCA enhances the grain fragmentation process and, as a consequence, reduces furthermore the crystal size.

The reduction in crystal size because of the milling time for the samples produced without PCA is of 2.8 nm, which corresponds to a 12% reduction when compared to the sample milled for 10 h. On the other hand, the samples produced with PCA presented a reduction of 6.5 nm, which corresponds to a 33% reduction when compared with the sample milled for 10 h with PCA. These reductions present similar values to results obtained by other authors when analyzing Fe–Co alloys obtained by MA.[45,46,48]

The results obtained for the microstrain (ε) also present similar tendencies for all samples (Table 1). As milling time increases, the microstrain also increases. This is due to the MA process, which favors the formation of internal stresses in the alloys, causing larger values of microstrain in the final samples. However, it must be noted that the samples produced with PCA present lower values of microstrain than those produced without it. Similarly to the crystal size, the microstrain for the sample milled for 50 h with PCA has a lower microstrain value than the sample milled for 10 h without PCA. Therefore, the use of C_6H_{12} as a PCA reduces the microstrain in the final powders.

Finally, the dislocation density for all six samples is analyzed. The dislocation density, ρ_d, for each sample is evaluated following Equation (1)[49]

$$\rho_d = 2\sqrt{3}\frac{\varepsilon^{21/2}}{L\beta} \tag{1}$$

where ε is the microstrain, L is the crystal size, and β is Burger's vector, which can be obtained from Equation (2)[50] for a BCC structure using the lattice parameter, a, obtained by using the Rietveld refinement method

$$\beta = \frac{a\sqrt{3}}{2} \tag{2}$$

As shown in Equation (1) and (2), the dislocation density is directly proportional to the microstrain and inversely proportional to the crystal size and lattice parameter. Therefore, the evolution of the dislocation density for different milling times depends on the tendencies described for each individual parameter (lattice parameter, crystal size, and microstrain). From the previous results presented in Table 1, it can be observed that lattice parameters and microstrain tend to values that are similar for

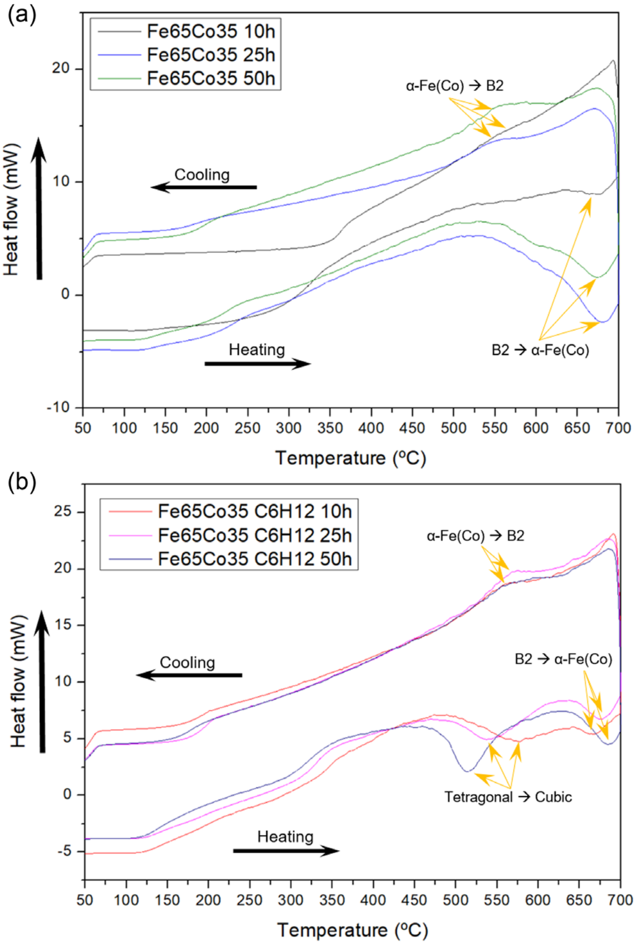

Figure 3. a) DSC curves for the samples produced without PCA and b) samples produced with PCA.

samples with and without PCA. However, the values of crystal size are significantly different between samples. As milling time increases, the difference between the crystal size of the sample with PCA and the sample without PCA increases. As a consequence, crystal size will determine the evolution of the dislocation density over different milling times. Therefore, as the crystal size for the samples with PCA is smaller, the dislocation density for these samples is larger (inversely proportional). This is true for milling times of 25 and 50 h; however, for 10 h, this is not the case. After 10 h of milling, the crystal size for both samples (with and without PCA) is close in value (3.74 nm difference). For lattice parameter and microstrain, the corresponding values are further away in value (lattice parameter is larger and microstrain is lower for the sample with PCA). With all the parameters considered, the dislocation density for the sample milled for 10 h with PCA is lower than the one for the sample milled without it.

2.2. Thermal Analysis

At low temperatures, the DSC curves of all samples present similar patterns (**Figure 3**). However, the use of a PCA favors a more uniform thermal behavior of the samples, especially during cooling, as observable in Figure 3. In the temperature range below 375 °C, all six samples present an exothermic growth related to structural relaxations and crystal growth. This is an expected behavior for alloys produced by MA.[2,51] As quantified by the microstrain obtained from the structural analysis, MA induces stress on the powders used to manufacture the alloys.

At higher temperatures, the thermal behavior of the samples produced with and without PCA presents a similarity. This similarity is a reversible atomic rearrangement at ≈680 °C. This is in accordance with the transformation indicated in the Fe–Co phase diagram.[41] This reversible atomic rearrangement is associated with the transition between the B2 phase and α-Fe(Co) when heating and from α-Fe(Co) to B2 when cooling. Nonetheless, the reversibility from α-Fe(Co) to B2 is not total. As observable in the DSC curves, the energy associated with the cooling transformation (α-Fe(Co) to B2) is lower than that for the heating (from B2 to α-Fe(Co)). The energy difference is due to a partial transformation from α-Fe(Co) to B2, where not all the α-Fe(Co) phase transforms into B2. These results are in accordance with the Fe–Co phase diagram provided in ref. [41]. The hysteresis of the reversible process is roughly 115 °C for all samples.

DSC also detects an additional endothermic peak during heating for the samples produced with PCA between 525 and 575 °C, depending on the sample. This peak is associated with the metastable superlattice of Fe_3Co.[32,52–56] The formation of this phase is well-known from steel manufacturing, with carbon promoting the formation of a tetragonal structured phase Fe_3Co ($P4/mmm$ space group and Strukturbericht designation $L6_0$),[46] which produces a metastable pattern of antiphase domains. A very similar situation might be happening in these samples, promoted by an increase in temperature.

2.3. SEM-EDX Observation

Figure 4 shows the SEM images of the powders obtained after MA by milling for different milling times. The images clearly show the effects of the different manufacturing parameters of the samples. As the milling time increases, the particle size decreases. Also, the homogeneity of the particle size increases with longer milling times. When the use of C_6H_{12} is analyzed, it is clear that it has a beneficial effect on particle size by favoring the obtaining of a smaller particle size in a reduced milling time,

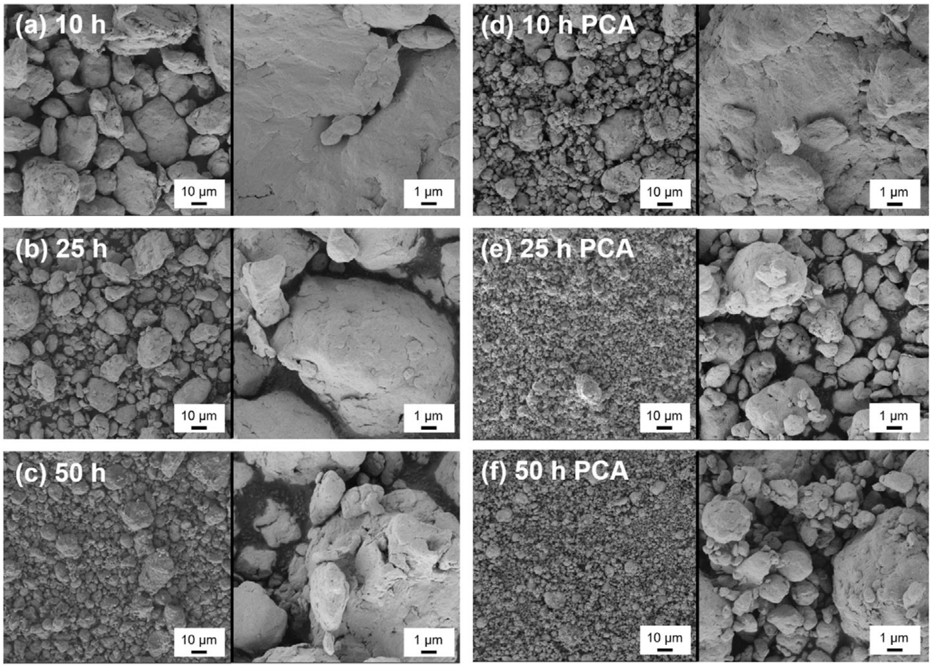

Figure 4. SEM images of $Fe_{65}Co_{35}$ powders obtained by mechanical alloying without PCA for milling times of a) 10 h, b) 25 h, and c) 50 h. d–f) The SEM images obtained for the powders milled for the same milling times and using PCA.

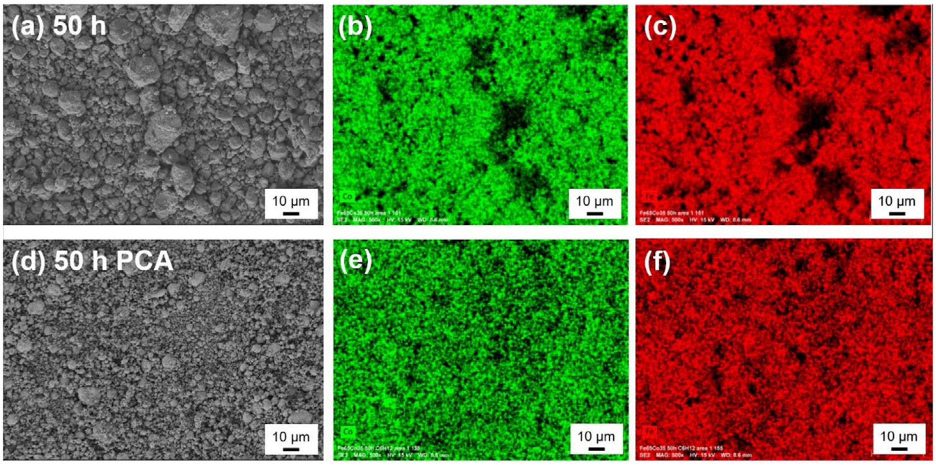

Figure 5. SEM images for samples milled for 50 h a) without PCA and d) with PCA. b,e) The Co distribution, and c,f) the Fe distribution obtained by EDX mapping in the $Fe_{65}Co_{35}$ alloy powders.

in addition to a more homogeneous distribution (reduced deviation around the mean particle size). When comparing the samples milled for the same time, it is clear that the particle size decreases when using the PCA during the milling. This is due to the fact that the main purpose of a PCA is to prevent the excessive cold welding of the powders used in the manufacturing of the alloy.[34–38]

EDX analyses of the samples confirm the nominal chemical composition of the alloys as $Fe_{65}Co_{35}$. It also confirms the homogenous distribution of both Fe and Co. **Figure 5** corresponds to the EDX results obtained for the samples milled for 50 h with and without C_6H_{12}.

2.4. Magnetic Characterization

Figure 6 shows the room temperature hysteresis loops measured by VSM while **Table 2** presents the values of coercivity (H_c), remanent magnetization (M_r), and saturation magnetization (M_s) obtained from the hysteresis loops.

The magnetic behavior for all samples is clearly a soft ferromagnetic behavior; however, there are some remarkable differences depending on the manufacturing conditions. When analyzing the samples produced without PCA, all magnetic parameters increase for longer milling times (Table 2). However, experimental data dispersion could explain the small increase in remanent and saturation magnetization between 25 and 50 h. The results from the structural analysis showed that for longer milling times, the crystal size was reduced (from 23 nm at 10 h to 21 nm at 50 h without PCA and from 20 nm at 10 h to 13 nm at 50 h with PCA), favoring coercivity, remanent magnetization, and saturation magnetization.[57–59]

The analysis of the three samples manufactured with PCA shows how the coercivity and the remanent magnetization follow the same trends as the samples produced without PCA. However, for these three samples, the saturation magnetization is lower when compared to the samples produced without PCA (Table 2). As XRD-calculated microstrain for the alloy milled with PCA is lower, this effect cannot be associated with the disordering of the cubic phase. The presence of cementite in the sample, which presents a hard magnetic behavior,[45,46] presumably causes this reduction. The study by Chaira et al.

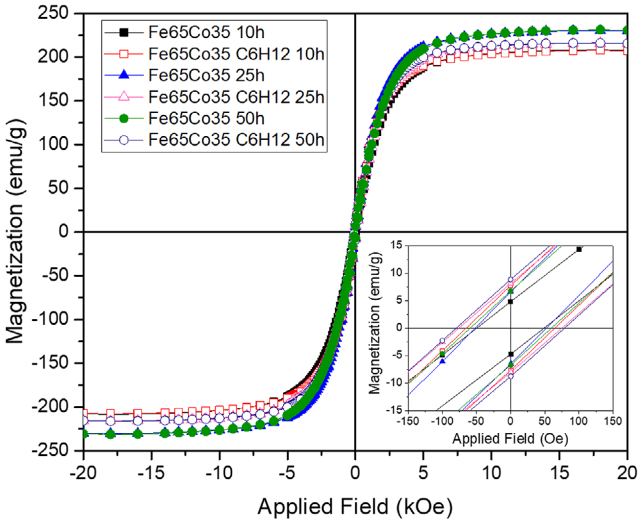

Figure 6. Magnetic hysteresis loops for all samples measured at room temperature by VSM.

Table 2. Main magnetic parameters obtained from the magnetic hysteresis loops: coercivity (H_c), remanent magnetization (M_r), and saturation magnetization (M_s).

Sample	H_c [Oe]	M_r [emu g^{-1}]	M_s [emu g^{-1}]
$Fe_{65}Co_{35}$ 10 h	49	4.8	208.0
$Fe_{65}Co_{35}$ 25 h	51	6.6	229.9
$Fe_{65}Co_{35}$ 50 h	59	6.7	230.8
$Fe_{65}Co_{35} + C_6H_{12}$ 10 h	65	7.7	207.3
$Fe_{65}Co_{35} + C_6H_{12}$ 25 h	76	8.1	215.6
$Fe_{65}Co_{35} + C_6H_{12}$ 50 h	80	8.8	215.6

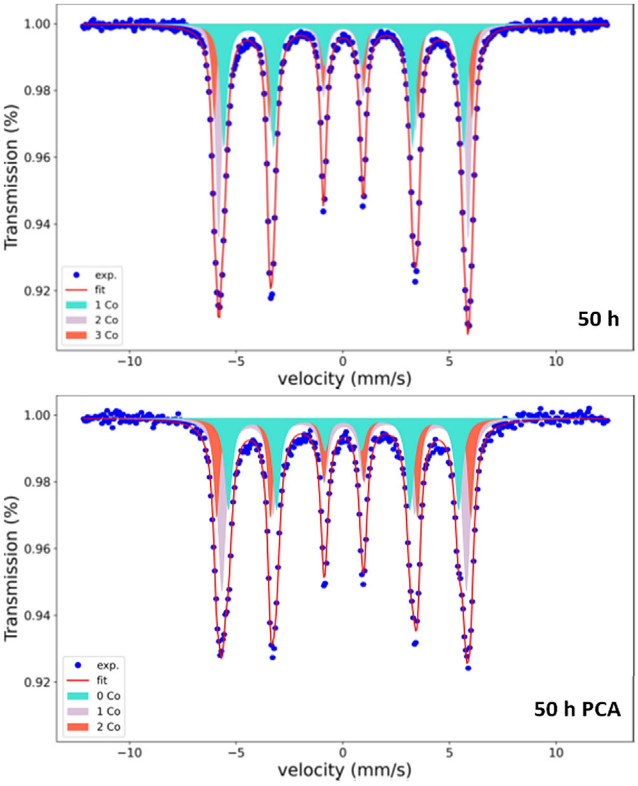

Figure 7. Mössbauer spectra for the samples milled for 50 h (top) and 50 h with PCA (bottom).

quantified a saturation magnetization of 80 emu g^{-1} and a coercivity of 325 Oe after 40 h of milling in a dual-drive planetary mill.[45] As the amount of cementite is low, the magnetic behavior of the samples will be less soft magnetic (i.e., higher values for H_c and M_r and lower values for M_s).

2.5. Mössbauer Spectroscopy

Mössbauer spectroscopy of the two samples milled for 50 h shows clear differences. The corresponding spectra and the hyperfine parameters are presented in **Figure 7** and **Table 3**.

Both spectra present the typical sextet pattern for ferromagnetic materials. Despite the detectable differences in the hyperfine parameters, they present the same characteristics. The peaks' widths are broader than the natural line and, therefore, one sextet is not enough to adjust the experimental data. In total, three different sextets were used to account for different environs surrounding the absorbing Fe nucleus. Three sextets were assigned to FeCo crystals in a BCC environ (corresponding to the crystal structure of the α-Fe(Co) phase) with an Fe nucleus surrounded by either 0, 1, 2 or 3 Co atoms as nearest neighbors (NN).[60] Both samples present very similar parameters, excluding the hyperfine fields and the quantity of each type of environ (Figure 7 and Table 3).

The main difference between samples is the values of the hyperfine field (BHF) of the three sextets. In general terms, the sample milled with PCA presents lower values (Table 3) than the sample without PCA. The lowest hyperfine field value for the PCA sample combined with the nearly zero isomer shift indicates that these hyperfine parameters are very similar to those corresponding to an α-Fe. This observation is different for the sample without PCA, as its lowest BHF value is higher and, therefore, does not present this sextet. This would imply that the Fe nucleus is not completely surrounded by Fe atoms (there is at least one atom of Co as a nearest neighbor). As mentioned previously, the use of PCA makes the diffusion of Co into the Fe matrix harder to achieve. Therefore, as expected for the sample milled with PCA, the amount of Co that has diffused into the Fe matrix is lower than that for the sample without PCA.

The sextet corresponding to having 1 and 2 atoms of Co as nearest neighbors is present in both samples. The last sextet corresponds with having 3 atoms of Co as the nearest neighbor

Table 3. Hyperfine parameters for the samples milled for 50 h and 50 h with PCA.

		50 h	50 h PCA			50 h	50 h PCA
0 Co NN	BHF [T]	–	33.4(5)	2 Co NN	BHF [T]	36.2(5)	36.9(5)
	δ [mm s^{-1}]		0.006(2)		δ [mm s^{-1}]	0.028(2)	0.026(2)
	Δ [mm s^{-1}]		0.01(1)		Δ [mm s^{-1}]	0.01(1)	−0.01(1)
	Γ [mm s^{-1}]		0.43(1)		Γ [mm s^{-1}]	0.36(1)	0.34(1)
	A13		2.9(1)		A13	3.0(1)	2.9(1)
	A23		1.6(1)		A23	1.5(1)	1.6(1)
	Area [%]		27.4(1)		Area [%]	44.0(2)	26.4(1)
1 Co NN	BHF [T]	34.8(5)	35.5(5)	3 Co NN	BHF [T]	37.4(5)	–
	δ [mm s^{-1}]	0.031(2)	0.033(2)		δ [mm s^{-1}]	0.028(2)	
	Δ [mm s^{-1}]	0.03(1)	0.01(1)		Δ [mm s^{-1}]	−0.02(1)	
	Γ [mm s^{-1}]	0.40(1)	0.48(1)		Γ [mm s^{-1}]	0.27(1)	
	A13	3.0(1)	2.9(1)		A13	3.0(1)	
	A23	1.5(1)	1.6(1)		A23	1.5(1)	
	Area [%]	34.7(2)	46.2(2)		Area [%]	21.3(2)	

(Figure 7). Only for the samples milled without PCA is this sextet detectable. The explanation is the same as for the α–Fe sextet. The effect of the PCA makes it harder for the diffusion of Co into the Fe matrix. Although both samples have a complete diffusion of Co in the Fe matrix, the atomic positions of Co are different in both samples. As Co diffusion is slower with PCA, it is harder for the B2 phase to form, thus probably favoring the minor local tetragonality. Therefore, as indicated in the structural analysis, the α-Fe(Co) structure is the predominant phase in the sample. The substitution of Co atoms causes the larger width of the spectra (Figure 7) when compared to the natural width of the α–Fe.[61–63]

Finally, the values of A13 and A23 in completely magnetic isotropic samples should be 3 and 2, respectively. For the samples of this study, the fitted value for A23 is ≈1.5 for both samples. The large dislocation density due to MA could cause this magnetic anisotropy.

3. Conclusions

$Fe_{65}Co_{35}$ powders have been synthesized by MA by milling for different times (10, 25, and 50 h). Two samples were manufactured per milling time, one of them with the addition of 1 mL of C_6H_{12} acting as a PCA. The structural, thermal, and magnetic characterization of all samples was carried out. The aim of the study was to analyze the effects of the synthesis conditions (milling time and the use of a PCA) on the characteristics of the resulting nanocrystalline $Fe_{65}Co_{35}$ alloy powders.

All results confirm that both the milling time and the use of a PCA alter the properties of the $Fe_{65}Co_{35}$ alloy. Longer milling times and the use of a PCA favor a major nanocrystallinity of the alloy. The use of a PCA additionally assists in the production of smaller particle sizes in a shorter milling time and enhances homogeneity in particle size distribution. Longer milling times enhance the diffusion of Co into the Fe matrix while the PCA slows this process down as it acts as a surfactant during milling. The use of the PCA also favors the formation of a tetragonal phase (Fe_3Co), confirmed by thermal analysis. From the magnetic characterization, longer milling times promote an increase in the magnetic properties (namely, coercivity and magnetization values). However, due to the presence of a hard magnetic tetragonal structure induced by the PCA, the behavior of these powder samples becomes less soft magnetic (higher coercivity and remanence and lower saturation magnetization).

This study has allowed to determine the effectiveness of using a PCA to reduce both the crystal and particle size with increasing milling times while making it possible to additionally tune the magnetic properties of $Fe_{65}Co_{35}$ alloy powders based on the choice of PCA. This possibility opens the path to designing nanocrystalline $Fe_{65}Co_{35}$ alloy powder with different morphological, microstructural, and magnetic properties in accordance with the requirements dictated by the final application requiring a high-performance soft ferromagnetic material.

4. Experimental Section

High-purity elemental powders were used in the manufacturing of the powder samples made of the soft magnetic alloy with a nominal composition of $Fe_{65}Co_{35}$. More specifically, a combination of Fe powder, with a purity of 99.5% and an average particle size below 10 μm, and Co powder, with a purity of 99.8% and an average particle size of 1.6 μm, were used (Alfa Aesar). A Fritsch Pulverisette P7 planetary ball milled the powders. The manufacturing conditions were milling at 400 rpm under an argon atmosphere with a ball-to-powder ratio (BPR) of 5:1 for different milling times. A higher BPR would cause the manufacturing process to be more energetic. This increase in energy favored the diffusion of Co into the Fe matrix and the evaporation of the PCA. However, the final sample presented more crystallographic defects. Therefore, the conditions were selected to favor the equilibrium between the temperature conditions needed for Co diffusion into the Fe matrix without increasing the crystallographic defects in the final sample. Three milling times were selected, namely 10, 25, and 50 h. Furthermore, 1 mL of C_6H_{12} was added to one of the samples for each of the milling times.

Structural analysis of the samples was carried out by X-ray diffraction (XRD) in a Bruker APEX D8 Advance diffractometer (Bruker, Billerica, MA, USA) using Cu-Kα radiation with an incident radiation wavelength of $\lambda = 1.5406$ Å, and the measurement range (2θ) was set between 30° and 120°. The obtained diffractograms were analyzed using the 2.9.9 version of MAUD software by applying the Rietveld Refinement Method, originally designed by H.M. Rietveld in 1969.[50] More specifically, the mathematical approach followed by the MAUD software was fitting the data of each diffractogram to a model crystallographic structure obtained from the Crystallography Open Database developed by Nick Day at the Department of Chemistry, University of Cambridge, under the supervision of Peter Murray–Rust. The approach employed the Rietveld Refinement Method using the Levenberg–Marquardt algorithm. The MAUD software read the experimentation parameters of the diffractometer and loaded them into the program. Then, the user had to upload the model crystallographic structure in the form of a CIF file (one file for each of the phases). By comparing the obtained diffractogram and CIF file, the program identified the angular positions of the peaks and obtained the lattice parameter of each phase in accordance with Bragg's Law and its relationship with the Miller Indices. Following the refinement of the lattice parameter, the program then calculates the average crystal size and microstrain of the sample by using the Williamson–Hall method for an isotropic sample. From the lattice parameter, average crystal size, and microstrain, the dislocation density for each sample could be calculated.[49] Finally, the program was capable of calculating the weight percentage of each phase from the area under the main peak of each phase.

Thermal analysis was performed by differential scanning calorimetry (DSC) in a TA Instruments Q2000 calorimeter (TA Instruments, New Castle, DE, USA). Samples underwent heating followed by cooling processes both in an argon atmosphere at a heating/cooling rate of 10 °C min^{-1}. The temperature range to analyze the samples was between 40 and 700 °C.

A Perkin Elmer EA2400 Series II device performed the elemental analysis of the samples and the Fe precursor. The temperature range for the combustion of the samples was between 925 and 930 °C using He as a carrier gas.

Morphological characterization of the samples was carried out by scanning electron microscopy (SEM) in a Zeiss EVO HD159, using a secondary electron detector at very low-pressure vacuum values of 10^{-6} hPa. Energy-dispersive X-ray analysis (EDX) determined the chemical composition of the samples by using ultrahigh-resolution SEM VP-Sigma EDX equipment (Bruker Nano XFlash Detector 430).

A Lakeshore 7400 series vibrating sample magnetometer (VSM) carried out the magnetic characterization of the samples under a maximum applied field of 20 kOe. Additionally, the samples milled for 50 h were analyzed by Mössbauer spectroscopy. The spectra were obtained at room temperature and pressure. A conventional constant acceleration spectrometer, in transmission mode, with a 25 mCi^{57}Co radioactive source in a Rh matrix was employed. The results were recorded in a standard multichannel analyzer using a speed range of ± 2.8 mm s^{-1} and fitted with the NORMOS software.

Acknowledgements

The authors acknowledge support by MICINN-AEI through the project *NEXUS* (PID2020-115215RB-C21 and PID2020-115215RB-C22). E.M.P. acknowledges support from AEI through the Juan de la Cierva–Incorporación program (grant IJC2020-043011-I/MCIN/AEI/10.13039/501100011033) and EU by NextGenerationEU/PRTR. IMDEA acknowledges support by MICINN-AEI through the "Severo Ochoa" Programme for Centers of Excellence in R&D (CEX2020-001039-S), and by the Regional Government of Madrid through the *NANOMAGCOST* project (S2018/NMT-4321).

Conflict of Interest

The authors declare no conflict of interest.

Authors Contribution

Jason Daza: data curation: (lead); formal analysis: (lead); investigation: (lead); and writing—original draft: (lead). **Zaida Curbelo-Cano**: data curation: (equal) and investigation: (equal). **Cristina M. Montero**: formal analysis: (equal) and investigation: (supporting). **Wael Ben Mbarek**: formal analysis: (equal) and investigation: (equal). **Lluïsa Escoda**: conceptualization: (lead) and supervision: (equal). **Joan Saurina**: investigation: (equal) and supervision: (supporting). **Ester M. Palmero**: conceptualization: (equal) and writing—review and editing: (equal). **Alberto Bollero**: conceptualization: (equal) and writing—review and editing: (equal). **Pere Bruna**: investigation: (equal) and writing—original draft: (supporting). **Joan Josep Suñol**: conceptualization: (lead) and writing—review and editing: (lead).

Data Availability Statement

Research data are not shared.

Keywords

Fe-based alloys, mechanical alloyings, process control agents, soft magnetics

Received: October 2, 2024
Revised: January 23, 2025
Published online:

---

[1] K. Suzuki, N. Kataoka, A. Inoue, A. Makino, T. Masumoto, *Mater. Trans.* **1990**, *31*, 743.
[2] J. Daza, W. Ben Mbarek, L. Escoda, J. J. Suñol, *Metals* **2021**, *11*, 1896.
[3] H. J. Ma, W. Q. Wei, W. K. Bao, X. B. Shen, C. C. Wang, W. M. Wang, *Rare Met. Mater. Eng.* **2020**, *49*, 2904.
[4] A. Carrillo, J. Daza, J. Saurina, L. Escoda, J. J. Suñol, *Materials* **2021**, *14*, 4542.
[5] B. Sai Ram, A. K. Paul, S. V. Kulkarni, *J. Magn. Magn. Mater.* **2021**, *537*, 168210.
[6] T. Kemény, D. Kaptás, L. F. Kiss, J. Balogh, I. Vincze, S. Szabó, D. L. Beke, *Hyperfine Interact.* **2000**, *130*, 181.
[7] T. Gheiratmand, H. R. Madaah Hosseini, *J. Magn. Magn. Mater.* **2016**, *408*, 177.
[8] D. Azuma, N. Ito, M. Ohta, *J. Magn. Magn. Mater.* **2020**, *501*, 166373.
[9] R. Coehoorn, D. B. de Mooij, J. P. W. B. Duchateau, K. H. J. Buschow, *J. Phys. Colloq.* **1988**, *49*, C8-669.
[10] E. F. Kneller, R. Hawig, *IEEE Trans. Magn.* **1991**, *27*, 3588.
[11] O. Gutfleisch, A. Bollero, A. Handstein, D. Hinz, A. Kirchner, A. Yan, K.-H. Müller, L. Schultz, *J. Magn. Mater.* **2002**, *242–245*, 1277.
[12] A. López-Ortega, M. Estrader, G. Salazar-Alvarez, A. G. Roca, J. Nogués, *Phys. Rep.* **2015**, *553*, 1.
[13] M. Estrader, A. López-Ortega, S. Estradé, I. V. Golosovsky, G. Salazar-Alvarez, M. Vasilakaki, K. N. Trohidou, M. Varela, D. C. Stanley, M. Sinko, M. J. Pechan, D. J. Keavney, F. Peiró, S. Suriñach, M. D. Baró, J. Nogués, *Nat. Commun.* **2013**, *4*, 2960.
[14] F. Magnus, M. E. Brooks-Bartlett, R. Moubah, R. A. Procter, G. Anderson, T. P. A. Hase, S. T. Banks, B. Hjörvasson, *Nat. Commun.* **2016**, *7*, 11931.
[15] P. Karipoth, A. Thirumurugan, *J. Appl. Phys.* **2016**, *120*, 123906.
[16] P. G. Ziogas, A. B. Bourlinos, P. Chatzopoulou, G. P. Dimitrakopulos, A. Markou, A. P. Douvalis, *Magnetochemistry* **2024**, *10*, 35.
[17] R. Ponce-Pérez, C. A. Corona-García, J. M. Galicia Hernandez, A. Reyes-Serrato, J. Perry Corbett, J. Guerrero-Sánchez, *ACS Omega* **2024**, *9*, 24721.
[18] F. Sánchez-De Jesús, A. M. Bolarín-Miró, C. A. Cortés Escobedo, G. Torres-Villaseñor, P. Vera-Serna, *J. Metall.* **2016**, *2016*, 1.
[19] A. N. Popova, Y. A. Zaharov, V. M. Pugachev, *Mater. Lett.* **2012**, *74*, 173.
[20] M. Delshad Chermahini, M. R. Rahimipour, A. H. Pakseresht, *Adv. Powder Technol.* **2014**, *25*, 462.
[21] J. Sort, J. Nogués, S. Suriñach, J. S. Muñoz, M. D. Baró, *Mater. Sci. Eng.: A* **2004**, *375–377*, 869.
[22] R. Parsons, B. Zang, K. Onodera, H. Kishimoto, A. Kato, K. Suzuki, *J. Alloys Compd.* **2017**, *723*, 408.
[23] A. M. Bolarín-Miró, F. Sánchez-De Jesús, G. Torres-Villaseñor, C. A. Cortés-Escobedo, J. A. Betancourt-Cantera, J. I. Betancourt-Reyes, *J. Non-Cryst. Solids* **2011**, *357*, 1705.
[24] L. D'Onofrio, G. González, D. Oleszak, A. Sagarzazu, R. Villalba, *Hyperfine Interact.* **2010**, *195*, 167.
[25] S. Bergheul, F. Otmane, M. Azzaz, *Adv. Powder Technol.* **2012**, *23*, 580.
[26] H. Laala-Bouali, F.-Z. Bentayeb, S. Louidi, X. Guo, S. Tria, J. J. Suñol, L. Escoda, *Adv. Powder Technol.* **2013**, *24*, 168.
[27] D. H. Manh, D. K. Tung, L. T. H. Phong, N. X. Phuc, P. T. Phong, J. Jutimoosik, R. Yimnirun, *J. Electron. Mater.* **2016**, *45*, 2501.
[28] H. Martínez Sánchez, L. E. Zamora Alfonso, J. S. Trujillo Hernandez, G. A. Pérez Alcázar, *J. Magn. Magn. Mater.* **2019**, *473*, 221.
[29] Z. Liu, R. J. Chen, Y. Ding, M. Z. Ding, D. Lee, A. R. Yan. *J. Appl. Phys.* **2010**, *107*, 09A702.
[30] T. Sourmail, *Scr. Mater.* **2005**, *52*, 1347.
[31] Y. Ustinovshikov, S. Tresheva, *Mater. Sci. Eng.* **1998**, *248*, 238.
[32] Y. Li, W. Qiang, *Comput. Mater. Sci.* **2022**, *202*, 111005.
[33] I. C. Cu, M. Doi, M. Sahashi, *J. Magn. Magn. Mater.* **2006**, *304*, e121.
[34] N. Yazdani, M. R. Toroghinejad, A. Shabani, P. Cavaliere, *Metals* **2021**, *11*, 1493.
[35] J. Shi, Z. H. Lin, Y. P. Liang, R. X. Li, Z. H. Cao, *Mater. Chem. Phys.* **2020**, *256*, 123728.
[36] M. A. Ruiz-Esparza-Rodríguez, C. G. Garay-Reyes, I. Estrada-Guel, J. L. Hernández-Rivera, J. J. Cruz-Rivera, E. Gutiérrez-Castañeda, C. D. Gómez-Esparza, R. Martínez-Sánchez, *J. Alloys Compd.* **2021**, *882*, 160770.
[37] A. Cotai, B. V. Neamtu, F. Popa, T. F. Marinca, O. Isnard, I. Chicinas, *J. Alloys Compd.* **2021**, *880*, 160497.
[38] A. Nouri, C. Wen, *Crit. Rev. Solid State Mater. Sci.* **2014**, *39*, 81.
[39] D. Papantonis, W. A. Bassett, *J. Appl. Phys.* **1977**, *48*, 3374.
[40] W. C. Ellis, E. S. Greiner, *Trans. Am. Soc. Met.* **1941**, *29*, 415.
[41] A. Taylor, R. W. Floyd, *Acta Crystallogr.* **1950**, *49*, 831.
[42] H. Okamoto, *J. Ph. Equilibria Diffus.* **2008**, *29*, 383.
[43] H. Asano, Y. Bando, N. Nakanishi, S. Kachi, *J. Japan Inst. Met.* **1966**, *30*, 684.

[44] I. Ohnuma, H. Enoki, O. Ikeda, R. Kainuma, H. Ohtani, B. Sundman, K. Ishida, *Acta Mater.* **2002**, *50*, 379.
[45] A. I. Rincón Soler, R. R. Rodríguez Jacobo, M. H. Medina Barreto, B. Cruz-Muñoz, *Hyperfine Interact.* **2017**, *238*, 48.
[46] D. Chaira, B. K. Mishra, S. Sangal, *J. Alloys Compd.* **2009**, *474*, 396.
[47] X. X. Bi, B. Ganguly, G. P. Huffman, F. E. Huggins, M. Endo, P. C. Eklund, *J. Mater. Res.* **1993**, *8*, 1666.
[48] M. Kezrane, A. Guittoum, N. Boukherroub, S. Lamrani, T. Sahraoui, *J. Alloys Compd.* **2012**, *536S*, S304.
[49] H. M. Rietveld, *J. Appl. Crystallogr.* **1969**, *2*, 65.
[50] A. Carrillo, J. Daza, L. Escoda, J. J. Suñol, *XRD Analysis: Rietveld Refinement And MAUD Software*, Spain **2022**.
[51] V. A. Bautin, S. A. Gudoshnikov, A. G. Seferyan, N. A. Usov, *J. Supercond. Novel Magn.* **2017**, *30*, 1281.
[52] J. Daza, W. Ben Mbarek, L. Escoda, J. Saurina, J. J. Suñol, *Technologies* **2023**, *11*, 78.
[53] D. W. Clegg, R. A. Buckley, *Met. Sci. J.* **1973**, *7*, 48.
[54] A. K. Seeger, *Int. J. Mater. Res.* **2006**, *97*, 861.
[55] S. Honjo, S. Kikuchi, A. Sakuma, S. Ishio, J. Balachandran, *J. Magn. Magn. Mater.* **2018**, *465*, 64.
[56] Y. Li, D. Yang, W. Qiang, *J. Magn. Magn. Mater.* **2023**, *565*, 170291.
[57] Y. Li, W. Qiang, K. Wang, D. Yang, B. Huang, F. Ding, *Mater. Sci. Eng. A* **2022**, *852*, 143718.
[58] A. V. Izotov, B. A. Belyaev, P. N. Solovev, N. M. Boev, *J. Magn. Magn. Mater.* **2021**, *529*, 167856.
[59] J. Liu, J. Wilson, C. L. Davies, A. Peyton, *J. Magn. Magn. Mater.* **2019**, *481*, 55.
[60] F. J. Gomes Landgraf, J. R. Filipini da Silveira, *J. Magn. Magn. Mater.* **2011**, *323*, 2335.
[61] N. Patelli, F. Cugini, D. Wang, S. Sanna, M. Solzi, H. Hahn, L. Pasquini, *J. Alloys Compd.* **2022**, *890*, 161863.
[62] R. Brand, *NORMOS-90 Mössbauer Fitting Program Package*, Laboratorium für Angewandte Physik, Universität Duisburg, D-4100 Duisburg, FRG, Stanberg, Germany **1990**.
[63] J. S. Blázquez, A. Conde, J. M. Grenèche, *J. Phys. Condens. Matter* **2003**, *15*, 7843.